

Report

AMESP - Phase 2 WP3



Title : AMESP - Phase 2 WP3

Authors : K. S. Moreira, Luewton L F Agostinho, R.H. Braga Leivas

Date : December 4, 2024

Code :

Version : 1

Status : draft

Mailing list :

Copy to :

Classification : confidential

Contents

1 WP3 Overview	2
1.1 Objectives	2
1.2 Timeline of Executed Tasks	2
1.3 Conventions	2
2 Current-based Classification and Control	3
2.1 Measuring the currents by spray mode	4
2.2 Reproducing Results from Verdoold et al. (2013)	6
2.3 Crown influences on i_{GND}	8
2.3.1 Atenuating Crown Influences on i_{GND}	8
2.3.2 8 vs 16 Needles in the Crown	9
2.4 Classifying the Spraying Mode	10
2.5 Optimizing the Signal Acquisition	11
2.6 Optimizing the Classification	14
2.6.1 Trying different statistical parameters	14
2.6.2 Classification via small Neural Networks	15
2.7 Proof-of-Concept Real-time EHDA Classification	16
2.8 Proof-of-Concept Real-Time EHDA Control	17
3 PID Controller Investigations	17
4 Other Results	19
4.1 Flow Rate disturbances	19
4.2 Relations between i_N , i_{GND} and i_C	20
4.3 Inrush Current on i_N Measurements	21
4.4 Switching i_N ON and OFF in a 2-second interval	22
References	24

1 WP3 Overview

1.1 Objectives

As stated on the proposal, we have two main goals in the WP3:

1. Investigate methods to identify the electrospray mode during operation by reading current values
2. Investigate methods to perform corrective actions to restore the electrospray operation by sending commands to the pump and/or power supply

We have explored two approaches that could achieve these goals, and they are detailed on Sections 2 and 3. For each approach, we discuss how they can be implemented in the system developed by Gilbert, their advantages and disadvantages, and how well they perform in achieving the above goals.

Section 4 shows some results obtained during the control investigations that were not directly used to achieve the goals of this Work Package, but we believe they could still prove useful to Gilbert and provide inputs to how the multinozzle prototype operates.

1.2 Timeline of Executed Tasks

Figure 1 shows a timeline of executed tasks for Work Package 3.

Tasks	July				August				September				October				November				December				
	1	2	3	4	1	2	3	4	1	2	3	4	1	2	3	4	1	2	3	4	1	2	3	4	
PID Controller Investigations																									
Time Response Analysis																									
Pump Disturbances																									
3 currents measurements																									
Reproducing Single Nozzle																									
Crown Influences Investigations																									
Classifying the spray mode																									
Optimizing the Classification																									
POC Real-Time EHDA Classification																									
POC Real-Time EHDA Control																									

Figure 1. Timeline of executed tasks.

The tasks on Figure 1 relate directly to the sections of this report in the table of contents. The gap between August and September corresponds to the holiday period of several members of the project. Tasks executed of other Work Packages are not included in the timeline.

1.3 Conventions

Throughout this report, we'll refer multiple times to physical variables of the system. Figure 2 shows the variable conventions we'll use in this text.

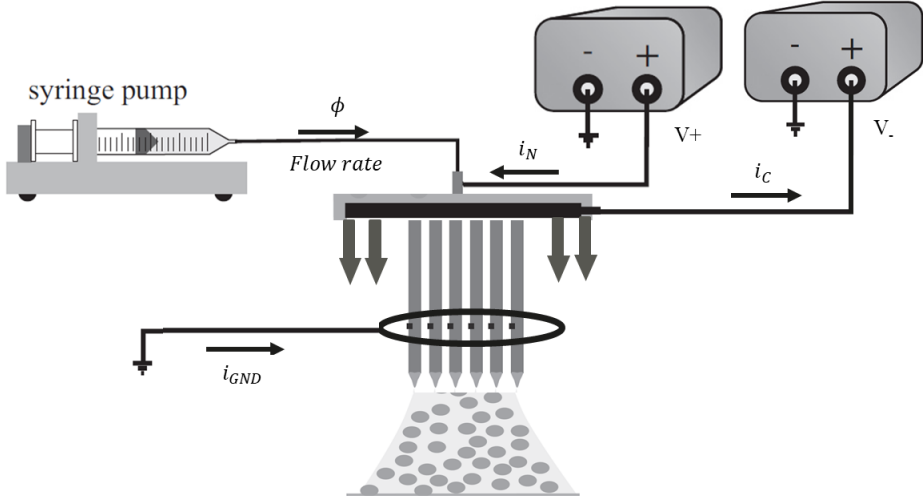


Figure 2. Variable conventions and nomenclature. Source: adapted from Verdoold et al. (2013).

As shown in Figure 2, we have

- i_N : current flowing from the positive high voltage source to the nozzles
- i_C : current flowing from the crown to the negative high voltage source
- i_{GND} : current flowing from the ground to the ring
- ϕ : flow rate of the syringe pump
- V_+ : voltage of the positive high voltage source
- V_- : voltage of the negative high voltage source

The direction of the currents was chosen as shown in Figure 2 to ensure they are always positive in the measurements, facilitating the analysis.

2 Current-based Classification and Control

The general strategy adopted in this approach is to first classify the electrospray mode by measuring the current values on the system, and then experimentally design a controller that can move from an intermittent to a cone-jet spray mode.

The classification method is based on the analysis made by Verdoold et al. (2013). However, Verdoold's method was designed for the single nozzle, and it is not clear if we can extend his classification to a multinozzle configuration. Therefore, part of this work includes an attempt to extend his classification method to the system developed by Gilbert.

2.1 Measuring the currents by spray mode

The first test done was to measure the current on all three lines of the sprayhead and verify if we see a pattern in the shape of current that can be used to classify the spray mode. Figure 3 shows the setup used for this test. V_- was fixed on $V_- = -4.5\text{kV}$.

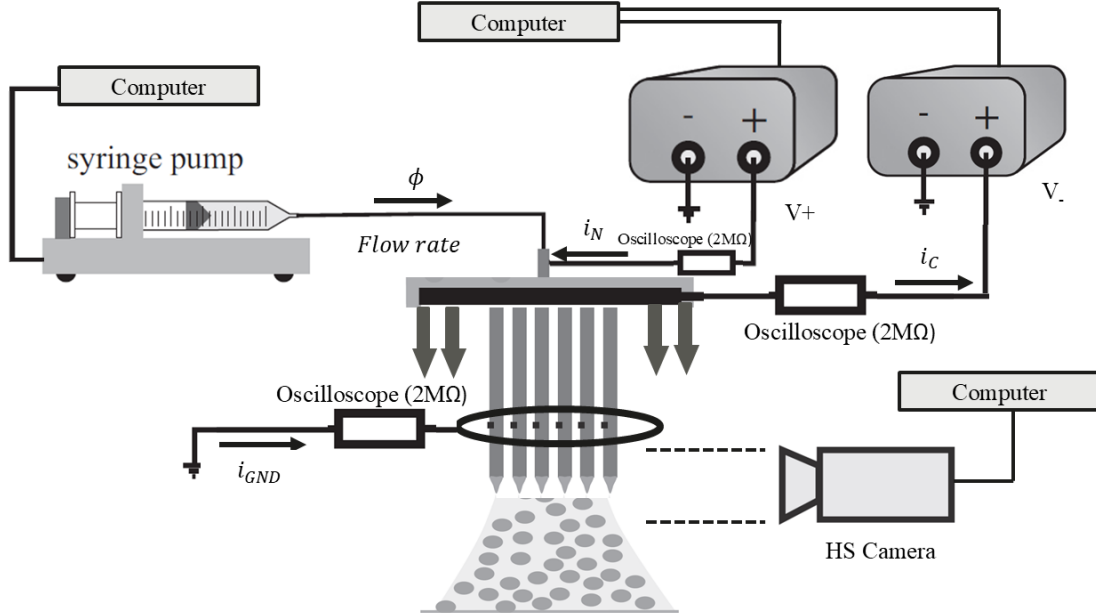


Figure 3. Setup to measure all three currents on the sprayhead. Source: adapted from Verdoold et al. (2013).

Using three oscilloscopes, all three currents were sampled at 5 kHz, collecting 20.000 samples of each (totalling a 4 seconds time window). Notice that, although the oscilloscope has multiple channels, we cannot use the same oscilloscope as the channels are interconnected internally: the high voltage differences would damage the instrument. Therefore, we use one oscilloscope for each line.

Since the oscilloscopes are in series, they will measure the voltage across the instrument. We know from the manufacturer's datasheet that the impedance of the oscilloscope is $Z_{in} = 2\text{ M}\Omega$. Therefore, using Ohm's Law, we can measure the current flowing through the oscilloscope with $i = \frac{\Delta V}{Z_{in}}$.

Furthermore, the addition of the oscilloscope in series does not cause a significant impact on the operation of the sprayhead. For instance, when we have a cone-jet at $i_N = 3\text{ uA}$ and $V_+ = 5\text{ kV}$, the impedance of the sprayhead Z_{sh} is

$$Z_{sh} = \frac{V_+}{i_N} = \frac{5\text{ kV}}{3\text{ uA}} = 1.6\text{ G}\Omega$$

Therefore, Z_{sh} is at least 3 orders of magnitude larger than Z_{in} , making the addition of the oscilloscope in series have a negligible impact on the operation of the sprayhead.

2.1 Measuring the currents by spray modeCurrent-based Classification and Control

We use the HS camera to identify the EHDA spray mode of the nozzles.

Figure 4 and Figure 5 show the waveforms obtained for $\phi = 20 \text{ mL/h}$; $\phi = 30 \text{ mL/h}$; $\phi = 50 \text{ mL/h}$ for two different time windows: 50ms and 500ms.

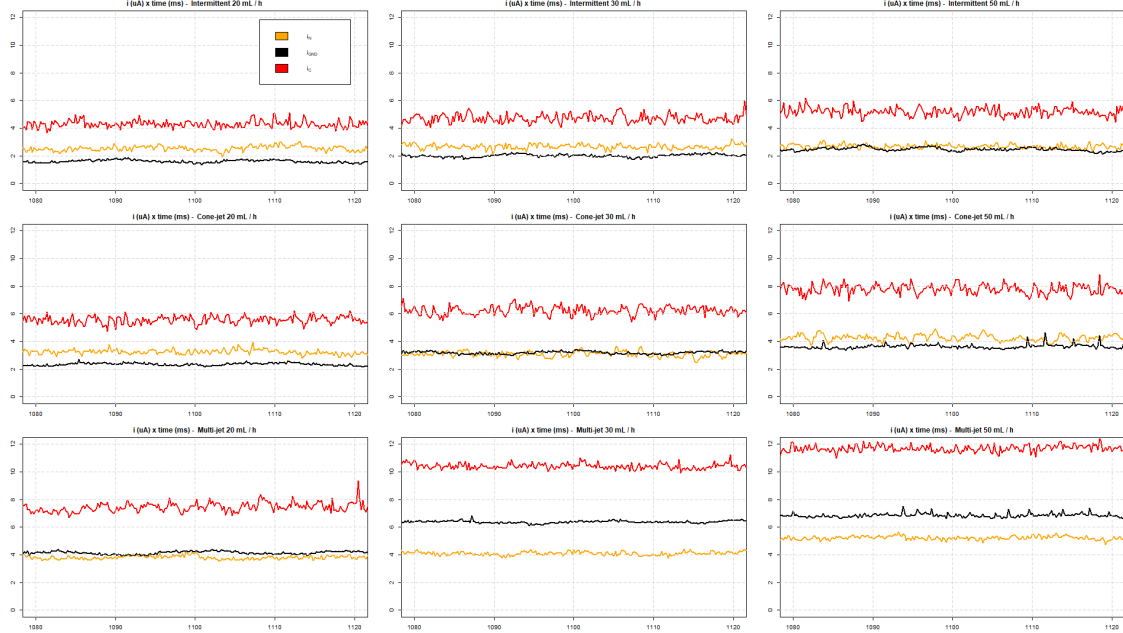


Figure 4. i_N , i_{GND} and i_C over time by different spray modes - 50 ms time window.

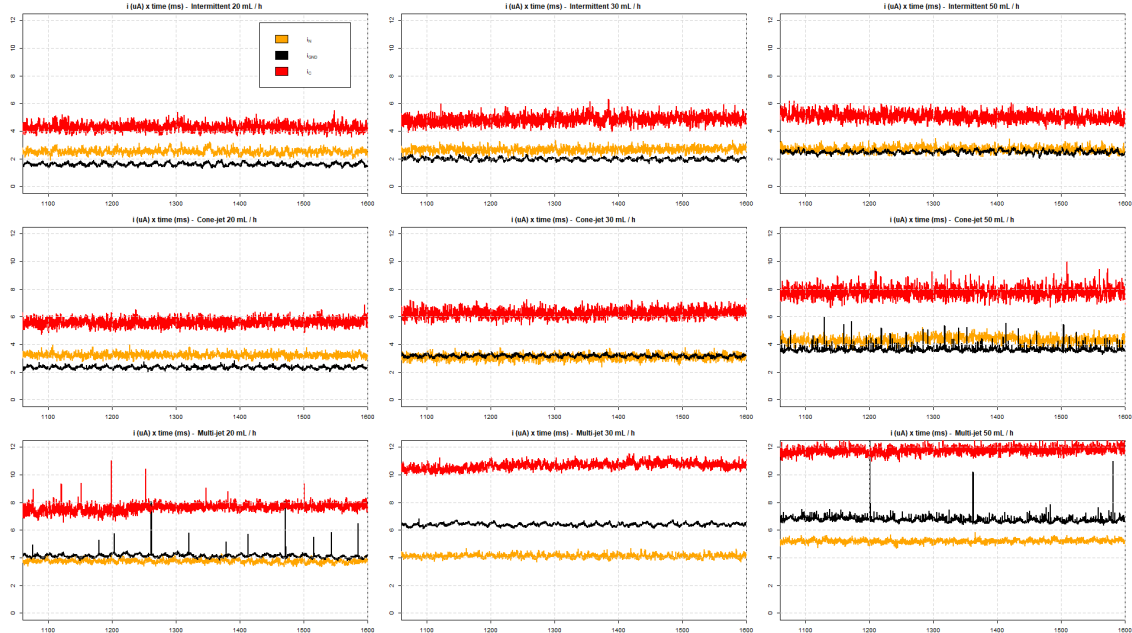


Figure 5. i_N , i_{GND} and i_C over time by different spray modes - 500 ms time window.

As we can see in Figure 4 and Figure 5, we don't see a clear distinction in the shape of the current by different spray modes, in both time windows. The sharp peaks we see on the waveforms are most likely caused by a high-frequency noise in signal,

especially since we use banana adapters for the oscilloscope in this test, instead of coaxial cables, which pick up less noise.

Attempting to see a distinction on Figure 5 via the standard deviation also fails, as shown on Figure 6.

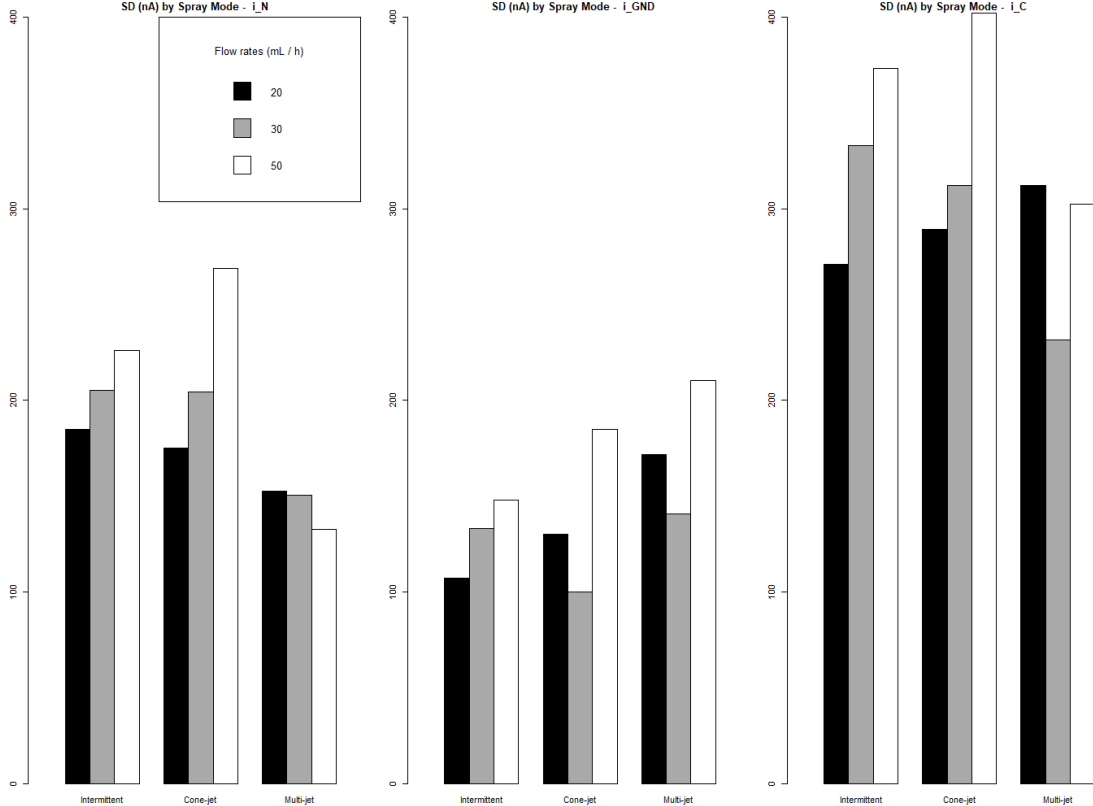


Figure 6. Standard deviation on Figure 5 of i_N , i_{GND} and i_C by spray mode.

Without a clear distinction in the current waveforms it would not possible to continue with this approach. Therefore, we need to first understand why we are not seeing distinctions in the shape of the current, particularly between the intermittent and cone-jet spray modes, as it is clear in the literature that there should be a difference.

To do this, we'll begin by attempting to reproduce Verdoold et al. (2013)'s results, with the goal of isolating if the problem is our measurement strategy or if it is something related to the sprayhead itself.

2.2 Reproducing Results from Verdoold et al. (2013)

Figure 7 shows the setup used to reproduce Verdoold et al. (2013)'s approach. We used a sampling frequency of 5 kHz and $\phi = 1 \text{ mL/h}$.

The results obtained are shown in Figure 8.

As we can see in Figure 8, we see a clear distinction between the spray modes,

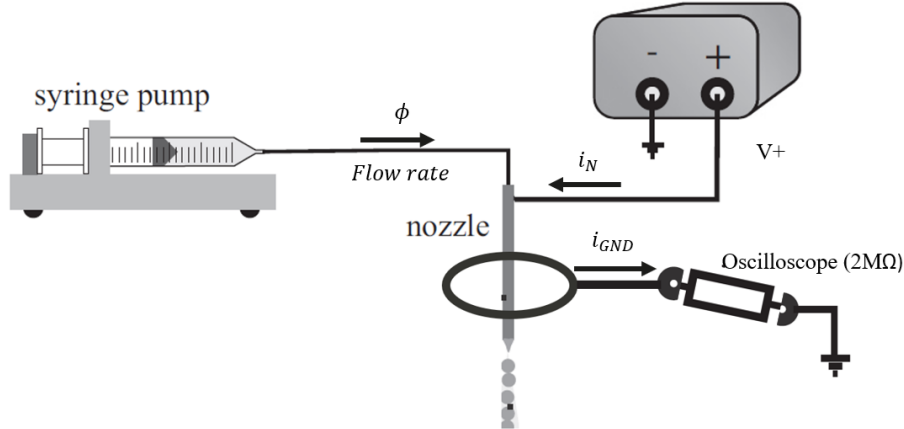


Figure 7. Setup used to reproduce Verdoold's classification method. Source: adapted from Verdoold *et al.* (2013).

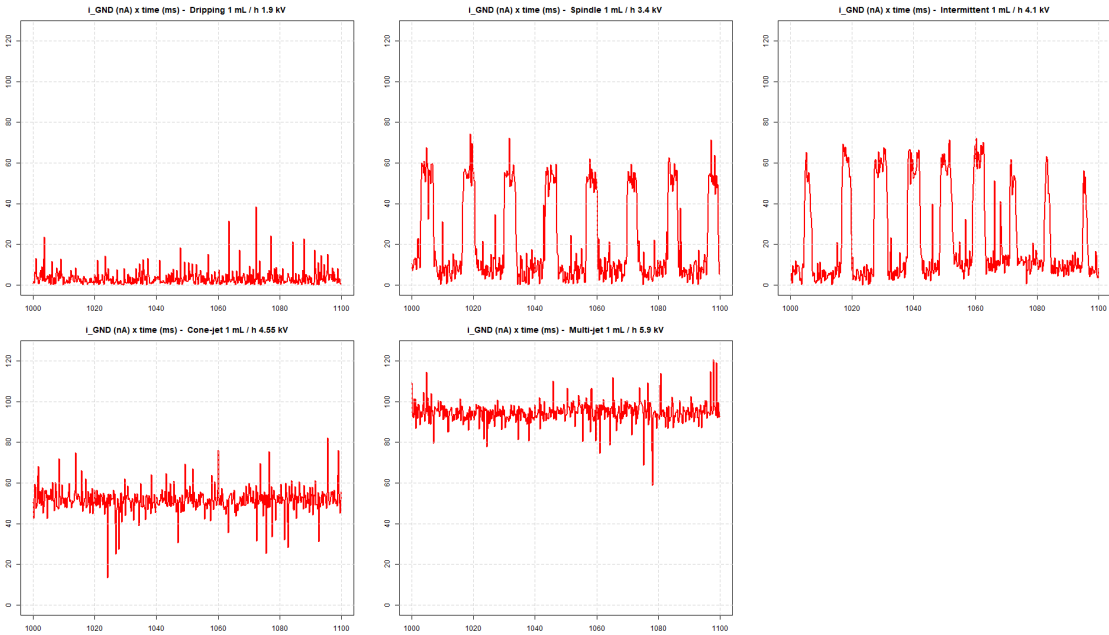


Figure 8. Results from the attempt to reproduce Verdoold's results on our setup.

which is what we wish to see in the multinozzle. We can conclude that our measurement methodology can reproduce the results, therefore it must be something in the multinozzle that is "hiding" the intermittent spray signal.

Comparing the single nozzle setup on Figure 7 and the multinozzle on Figure 3, the most significant difference is indeed the presence of the crown. Therefore, let's begin by understanding the influence of the crown on i_{GND} , which is the current that we know is capable of showing a distinction of spraying modes.

2.3 Crown influences on i_{GND}

To understand the influence of the crown on the ground current, we'll use the same setup shown on Figure 3, but we'll make $V_+ = 0\text{ V}$, $\phi = 0\text{ mL/h}$ and measure i_{GND} for different crown voltages. Since there is no flow and no positive voltage, we'll be measuring the current on the ground ring introduced by the crown only. In addition, we'll use coaxial cables during the measurements.

Figure 9 shows the shape of i_{GND} for different values of V_- .

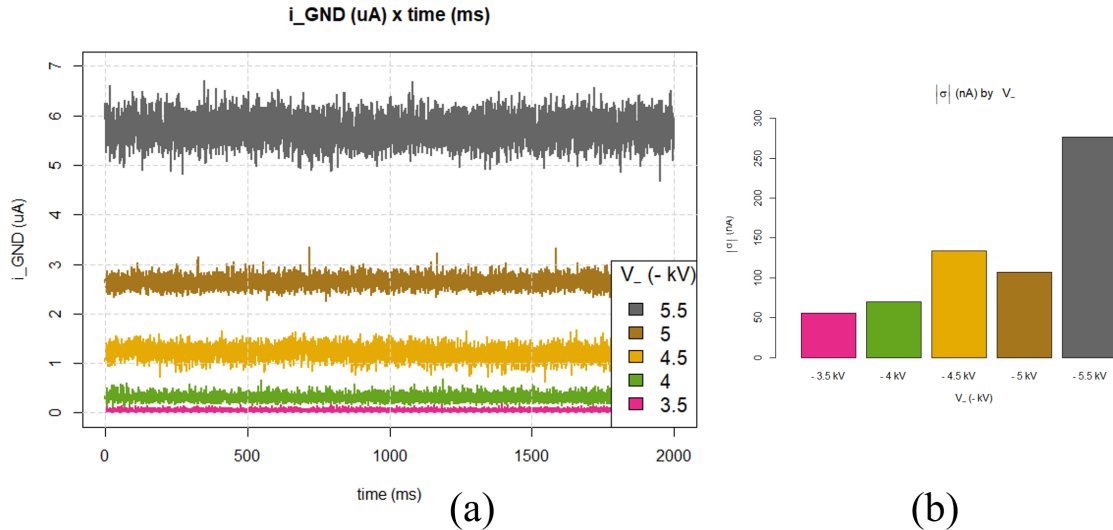


Figure 9. i_{GND} for different values of V_- . (a) Waveform and (b) standard deviation

As seen on Figure 9 (a), the crown alone introduces a signal on i_{GND} starting from $V_- = -4\text{ kV}$, which increases in both average value and standard deviation as V_- increases. This is consistent with what happens at the crown: from $V_- = -4\text{ kV}$ onwards the sharp needles of the crown begin to ionize the air, producing ions that can be directed to ground ring. This results in a current $i_{GND} > 0$ induced by the crown.

In addition, on Figure 9 (b) we see that the standard deviation introduced by the crown is significant. As we saw on Figure 8, the intermittent spray mode presents peaks in the current signal in order of 50 nA, but the "noise" introduced by the crown alone is already over 50 nA when $V_- = -4.5\text{ kV}$, which is the voltage used on the results of Figure 5. Therefore, it is reasonable to assume that the reason we are not seeing a good distinction between the spray modes on Figure 5 is because of this signal introduced by the crown alone.

2.3.1 Attenuating Crown Influences on i_{GND}

In order to verify the above hypothesis, we can try to reduce the influence of the crown in the signal and verify if the intermittent signal becomes distinguishable.

We can achieve this adding digital filters in the oscilloscope software to remove the following frequencies:

- 50 Hz frequency from the electric grid: use a stop band in the range 48 - 52 Hz
- All frequencies above 100 Hz: use low pass filter with cut-off frequency 100 Hz.

Since the intermittent peaks are usually under 100 Hz (Verdoold et al., 2013), we can remove anything above this frequency from the signal as it is not what we wish to measure.

Using this, we once again collect the signals of Figure 9, obtaining the signal on Figure 10.

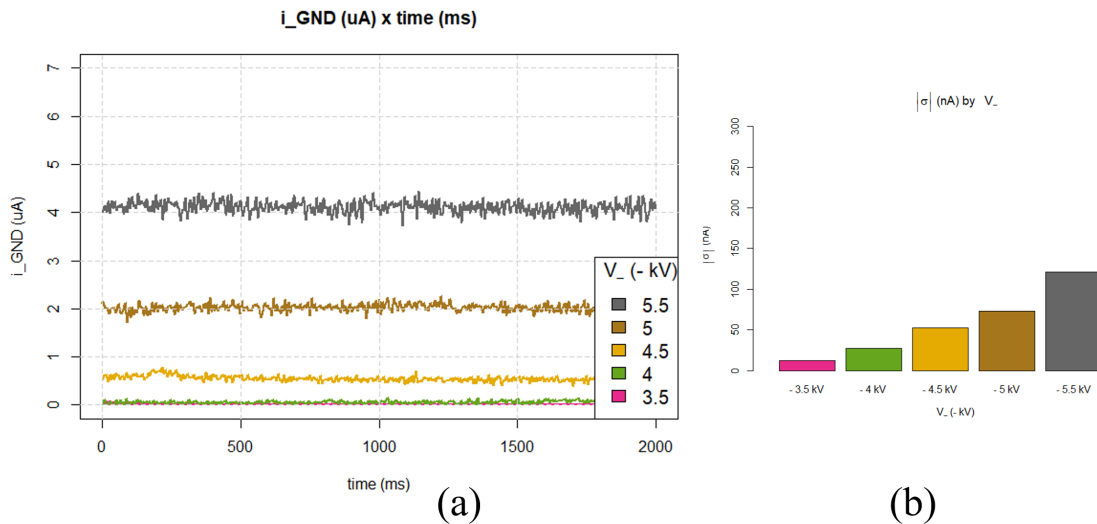


Figure 10. i_{GND} for different values of V_- with digital filters. (a) Waveform and (b) standard deviation

Comparing Figure 10 and Figure 9, we see that the filters significantly reduce the standard deviation (i.e. the "noise") in i_{GND} . For $V_- = -4.5$ kV, the standard deviation is already almost three times smaller. However, it remains above 50 nA, so it could still make it difficult to see the intermittent peaks in the signal. Ideally, we would use the $V_- = -4$ kV to get the smallest amount of noise introduced, but it is not clear if it is possible to achieve a good neutralization with such a small V_- .

2.3.2 8 vs 16 Needles in the Crown

Around this time, Gilbert requested us to test the crown with 8 needles for the WP2, as opposed to the 16 needles we had always used until this point. Difficulties to reinsert removed needles meant that from this point onwards we would always use a needle with 8 needles.

Therefore, before we continue with this analysis, we need to understand how the signal introduces on i_{GND} has changed. We've re-done the test of Figure 10, obtaining the results shown on Figure 11

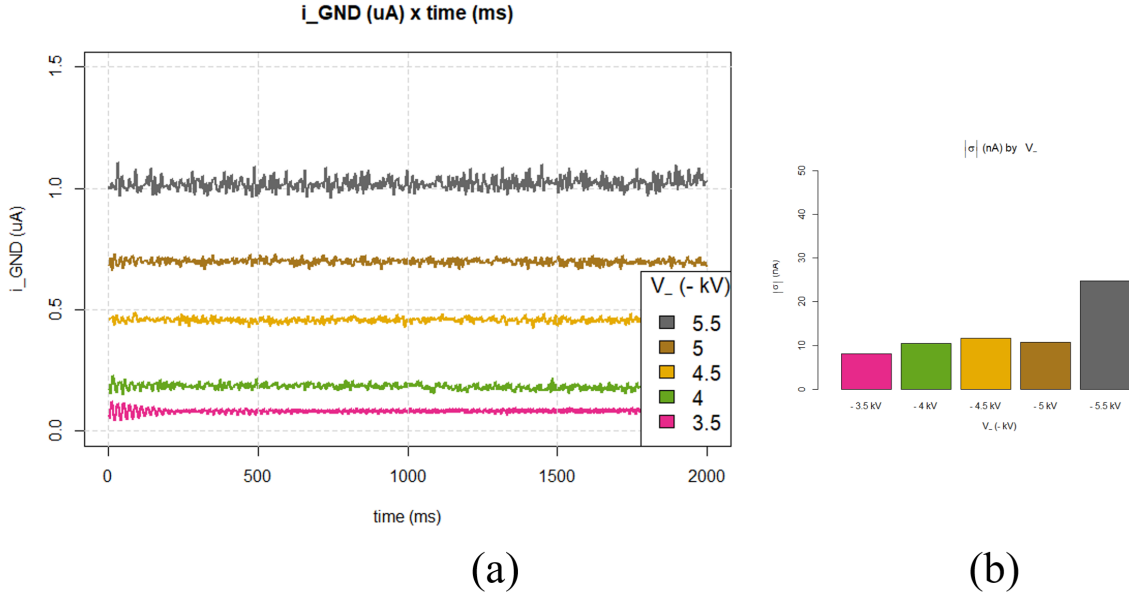


Figure 11. i_{GND} for different values of V_- with digital filters - Crown with 8 needles. (a) Waveform and (b) standard deviation

Comparing Figure 10 and Figure 11, we see that the 8 needles introduce a much smaller signal on the i_{GND} , both in terms of average value as in standard deviation. This will be helpful to make the intermittent peaks on the signal more visible, as for $V_- = -4.5 \text{ kV}$ the introduced standard deviation is only 10 nA.

2.4 Classifying the Spraying Mode

With everything that we've now learned about the influence of the crown and the necessity of filters, we can now repeat the experiment of Figure 3, using the same setup of Figure 3, but again only measuring i_{GND} . The oscilloscope was configured with $f_s = 5 \text{ kHz}$ and a sample size of $N_s = 20.000$. The crown had 8 needles and was fixed with $V_- = -4 \text{ kV}$ to reduce as far as possible the influence of the crown on i_{GND} .

Figure 12 shows the result obtained. The intermittent is clearly distinguishable from the cone-jet mode. However, expected, we cannot distinguish the elongated cone-jet and the multi-jet from the cone-jet.

Calculating the standard deviation on Figure 12 also allows for a good distinction between the spraying modes, as shown in Figure 13.

Based on Figure 13, we could use a simple if-else classification algorithm based on the standard deviation, defining a threshold for what is classified as intermittent or cone-jet. For example, we could say that if $\sigma > 60 \text{ nA}$ then it is intermittent, else it

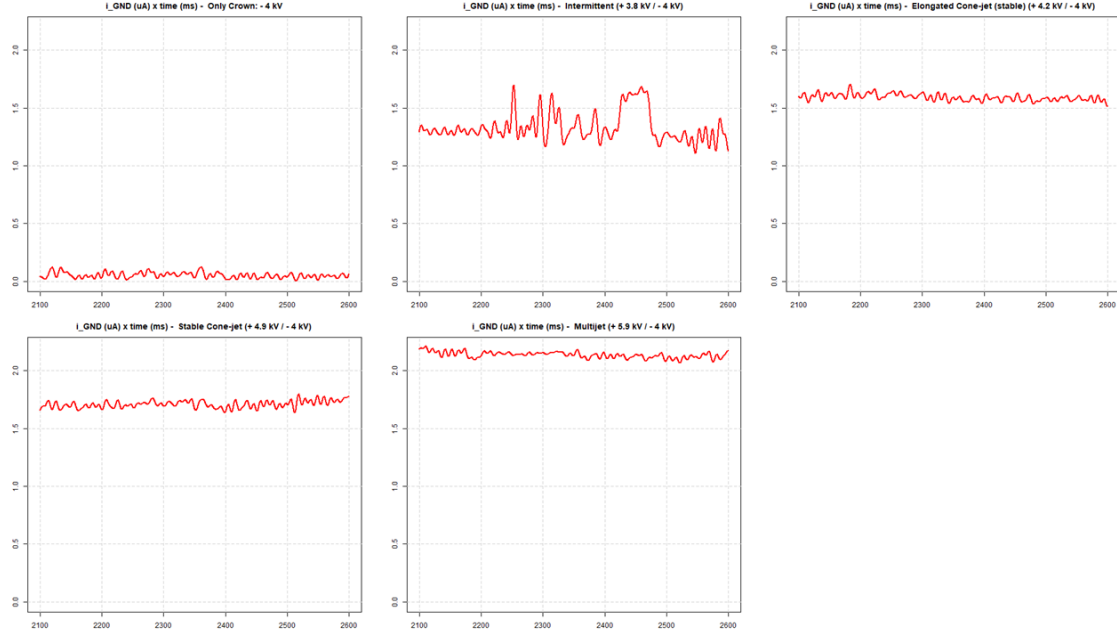
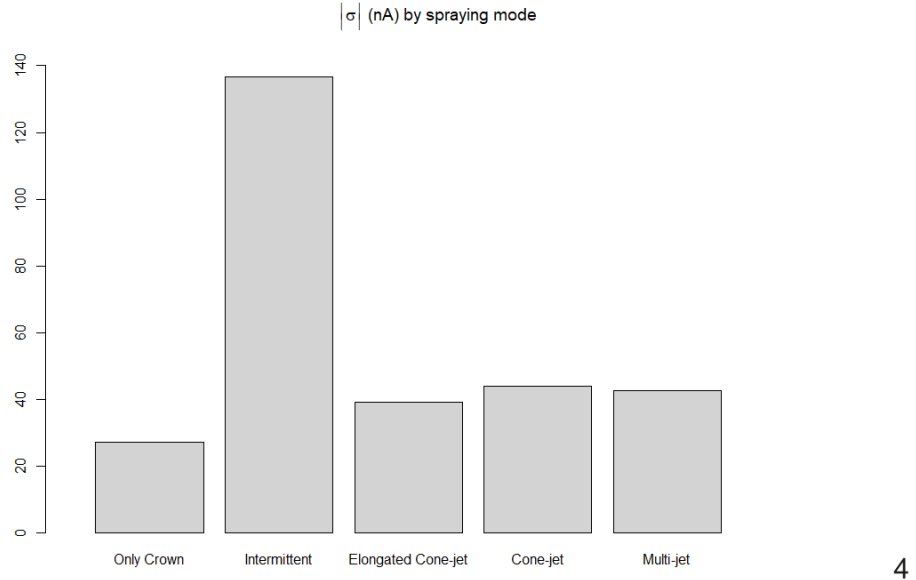


Figure 12. i_{GND} for different spray modes.



4

Figure 13. Standard deviation of i_{GND} for different spray modes.

is cone-jet (once inside the stable region defined by the mapping of the WP1). An algorithm for this will be further explored on subsection 2.7.

2.5 Optimizing the Signal Acquisition

In the previous sections, the signal was acquired using the minimum sampling frequency suggested by the Verdoold et al. (2013) of $f_s = 5\text{ kHz}$. A sample size of $N_s = 20.000$ was used to obtain a spectral resolution of 0.25 Hz for frequency do-

main analysis, also suggested by Verdoold as the minimum. However, talks with Gilbert showed that the sampling frequency was too computationally expensive and the sample size was too slow, as it resulted in a sampling time window of 4 seconds, which is too large.

Therefore, to attempt to meet these requirements, we need to find the minimum sampling frequency and minimum sample size that can still reliably distinguish the signal of the intermittent from the cone-jet.

To do this, we'll use the following method:

- Collect a time window of $T = 100$ seconds for different values of f_s , resulting in a sample size of $N_s = T \cdot f_s$
- Break the $T = 100$ seconds into smaller time windows - denoted as S_i - of size T_S .
- Calculate the relevant statistical parameters in each S_i and store these values in an array of size T/T_S
- Plot a boxplot of the calculated statistical parameters

Figure 14 further explains the method above visually. T_S will be chosen for different values for the result to be verified. Note that $i = 1, 2, \dots, T/T_S$, and the goal is to find the minimum T_S .

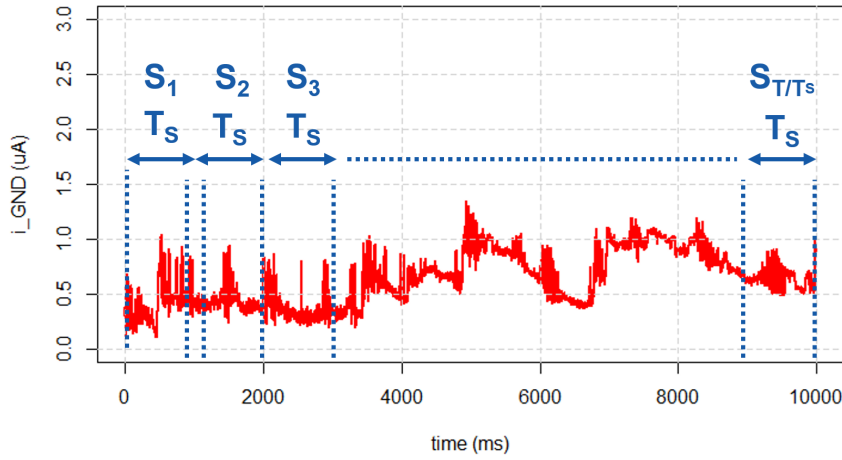


Figure 14. Method to find the minimum sample size that can still classify the EHDA mode via the current.

We'll use the same setup shown in Figure 3, using only the oscilloscope for i_{GND} . We begin with $f_s = 5$ kHz, with $T_S = 0.01$ s; 0.1 s; 1 s; 10 s. Note that we are first changing T_S over four orders of magnitude to understand the general influence of T_S on the calculated standard deviation. The result obtained is shown on Figure 15.

As we can see on Figure 15, $T_S = 1$ s appears to be the best sample size to differentiate between the intermittent and the cone-jet. Other orders of magnitude of T_S do not allow for a clear distinction between spraying mode via the statistical

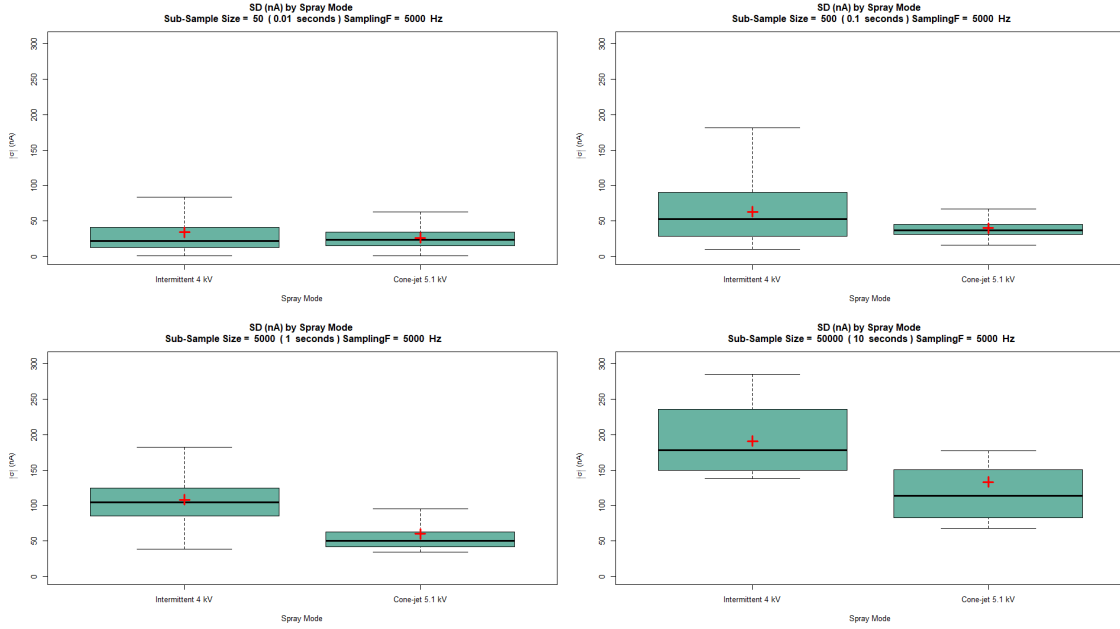


Figure 15. Calculated standard deviation for $f_s = 5\text{ kHz}$, with $T_S = 0.01\text{ s}; 0.1\text{ s}; 1\text{ s}; 10\text{ s}$

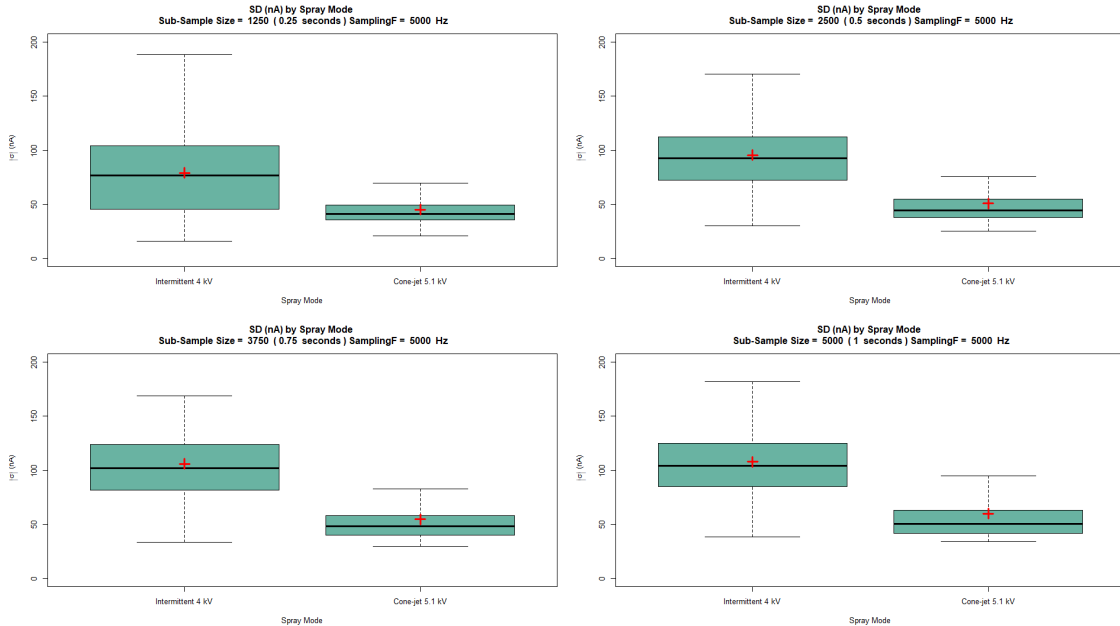


Figure 16. Calculated standard deviation for $f_s = 5\text{ kHz}$, with $T_S = 0.25\text{ s}; 0.5\text{ s}; 0.75\text{ s}; 1\text{ s}$

values. The next test is to change T_S around 1 second and compare them, using $T_S = 0.25\text{ s}; 0.5\text{ s}; 0.75\text{ s}; 1\text{ s}$. Figure 16 shows the results obtained for this test.

As seen on Figure 16, $T_S = 0.5\text{ s}$ appears to be the smallest sample size that can differentiate the spraying modes. $T_S = 0.5\text{ s}$ may still be feasible, but it presents significant overlapping between the two modes around $\sigma = 50\text{ nA}$.

Now we need to find the minimum sampling frequency that can distinguish the

spraying modes. We'll fix $T_S = 0.5$ s and compare the calculated statistical parameters for the following values of f_s : $f_s = 0.5$ kHz; 1 kHz; 2 kHz; 5 kHz. Figure 17 shows the result obtained for this test.

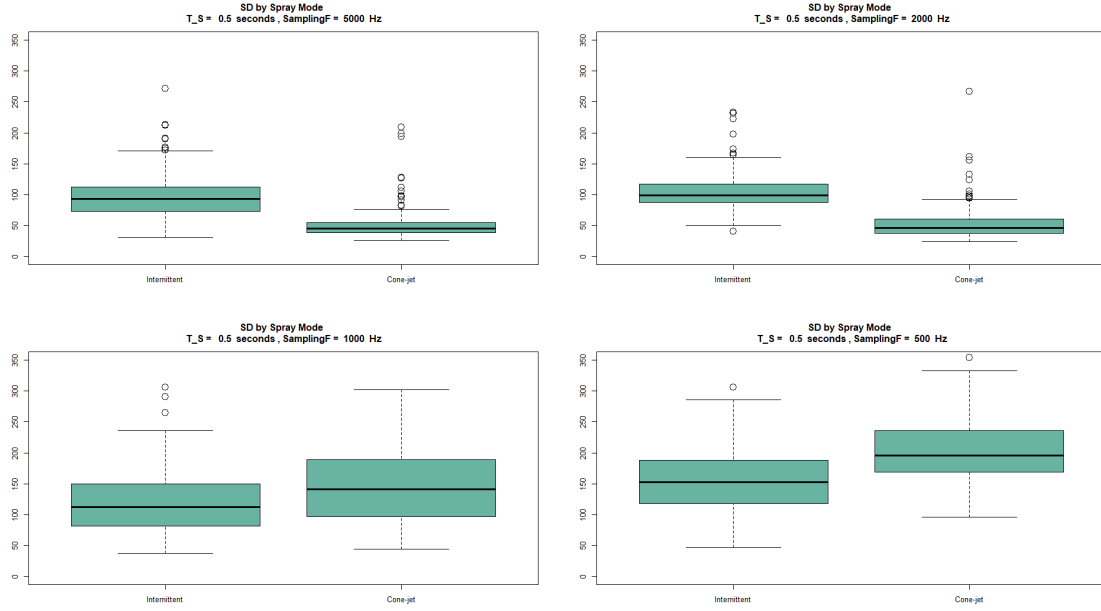


Figure 17. Calculated standard deviation for $T_s = 0.5$ s, with $f_s = 0.5$ kHz; 1 kHz; 2 kHz; 5 kHz

As we can see on Figure 17, $f_s = 2$ kHz appears to be the smallest sampling frequency that can still distinguish the spraying modes.

The conclusion we can derive from these tests is that $T_S = 0.5$ s and $f_s = 2$ kHz are the minimum sample size and sampling frequency that can distinguish the spraying modes via statistical parameters. Note that this results in a sample size of $N_s = T_S f_s = 1.000$, which uses significantly less memory than the $N_s = 20.000$. We'll move forward with these values of N_s and f_s , seeking to test the classification with parameters that are consistent with Gilbert's requirements.

2.6 Optimizing the Classification

2.6.1 Trying different statistical parameters

So far, we've only used the standard deviation of the signal to differentiate the spraying modes. However, we can also use other statistical parameters to distinguish the waveforms. The first one that we can try is the Relative Standard Deviation (RSD), defined on Equation 1

$$RSD = \left| \frac{\sigma}{\bar{I}} \right| \quad (1)$$

where

- σ : standard deviation
- \bar{I} : arithmetic mean

Table 1 shows how the RSD can be a useful metric in the classification. When the spraying mode is intermittent, we expect the signal to display a large σ and a small \bar{I} , since the potential is lower and therefore also the mean value of the current in the system. This results in an overall value large value of the ratio.

Table 1. Expected behaviour of RSD for different spraying modes.

	Intermittent	Cone-jet
Numerator (σ)	HIGH	LOW
Denominator (\bar{I})	LOW	HIGH
Overall Ratio (σ/\bar{I})	LARGE	SMALL

On the other hand, when we have a cone-jet, we expect the signal to display a small σ - as the signal is much more stable - and a larger \bar{I} , given the larger potential. This results in an overall value small value of the ratio.

Therefore, both components of the fraction contribute in opposite directions to change the overall value of the ratio between the spraying modes, making this metric a potentially good classification parameter.

Figure 18 shows the same result of Figure 17 using the RSD instead of the standard deviation.

As we can see on Figure 18, we can achieve a good distinction between the spraying modes with the RSD. However, the order of magnitude of the value is very small, which can be inconvenient. A simple to resolve this is take the inverse of the RSD, that we can define as the Signal-to-Noise Ratio (SNR), shown on Equation 2

$$SNR = \frac{1}{RSD} = \left| \frac{\bar{I}}{\sigma} \right| \quad (2)$$

In Equation 2, we call the standard deviation as the "noise", and the mean as the "signal". Figure 19 shows the same result of Figure 17 using the SNR.

As seen on Figure 19, the SNR is also a good metric to distinguish the intermittent and cone-jet modes. Unlike the RSD, the SNR spreads from the range 0 - 50, making it more convenient than the RSD and showing less outliers. Therefore, the RSD will be used from this point on, using $f_s = 2\text{kHz}$ and $N_s = 1.000$ ($T_s = 0.5\text{s}$).

2.6.2 Classification via small Neural Networks

ASK BEN

2.7 Proof-of-Concept Real-time EHDA Classification and Control

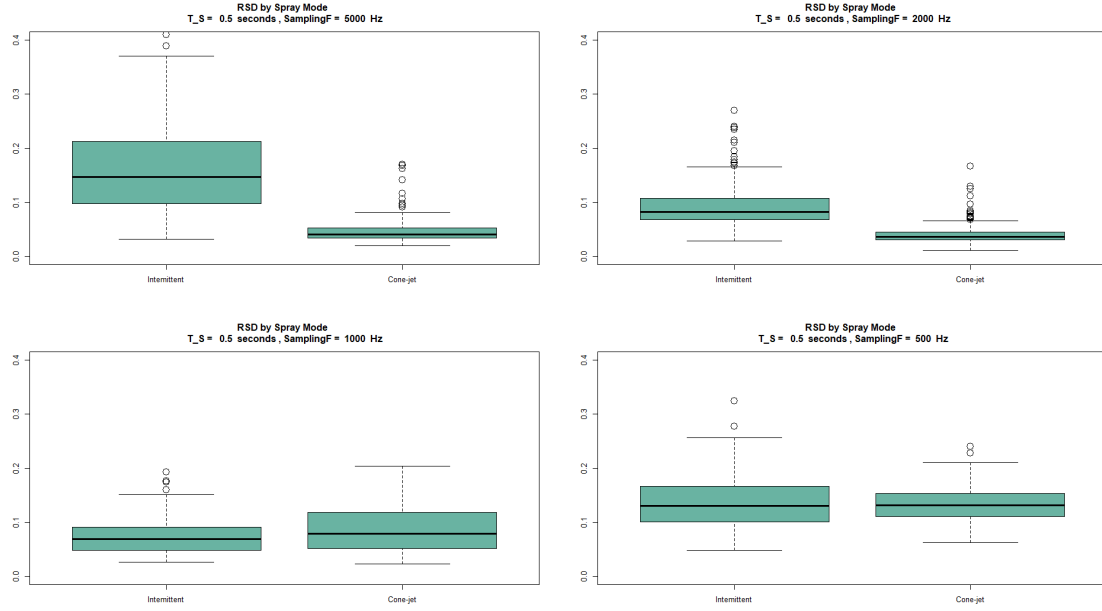


Figure 18. Calculated RSD for $T_s = 0.5\text{ s}$, with $f_s = 0.5\text{ kHz}; 1\text{ kHz}; 2\text{ kHz}; 5\text{ kHz}$

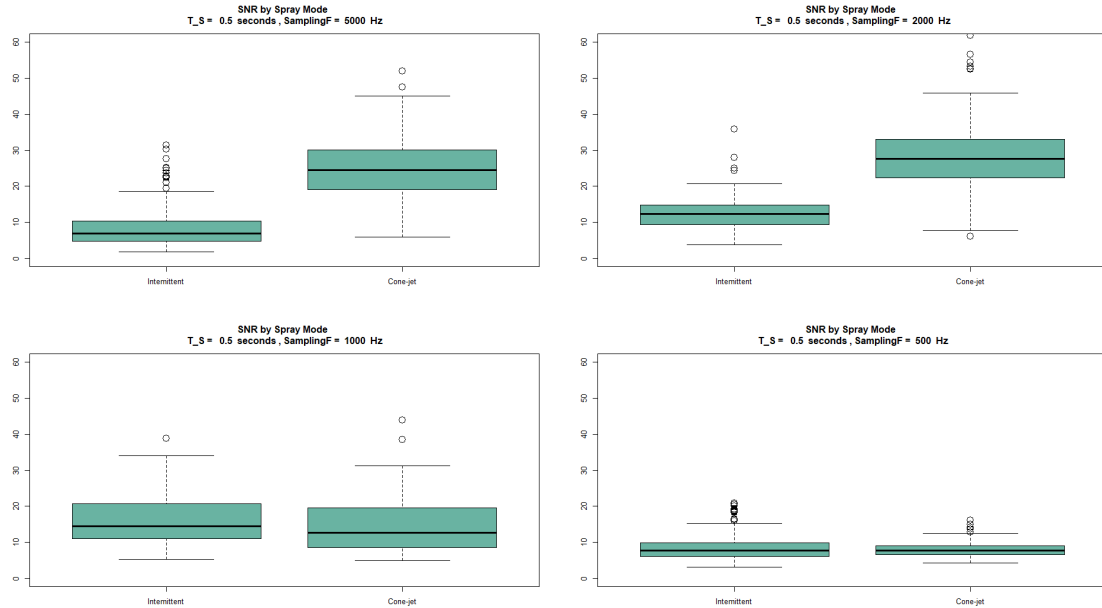


Figure 19. Calculated SNR for $T_s = 0.5\text{ s}$, with $f_s = 0.5\text{ kHz}; 1\text{ kHz}; 2\text{ kHz}; 5\text{ kHz}$

2.7 Proof-of-Concept Real-time EHDA Classification

TODO

- try to reduce sample window
- use subsequent windows

- show common issues (step in the current value, etc)
- add pseudocode + complexity

2.8 Proof-of-Concept Real-Time EHDA Control

TODO

- problem wth subsequent window: how will it take into account the adjusts we're making:
- is it fast enough? if it even works at all!
- add pseudocode + complexity

3 PID Controller Investigations

Based on the mappings done for the Work Package 1, given certain boundaries of V_+ , we can know if the spraying mode of the nozzles is a cone-jet if the mean value of i_N is in a certain range. Therefore, a first and simple attempt that we make to control the EHDA spray mode of the nozzles is ensure that i_N is always within this stable zone.

To achieve this, we can use a PID controller to ensure i_N is always in the center of the stable zone. The designed control loop is shown on Figure 20. The control system is provided a setpoint, which is value of i_N that it will attempt to keep fixed. In this sense, the controller will reject disturbances in order to keep i_N always equal to the setpoint. Therefore, it would ensure that the sprayhead is operating the in stable region mapped on WP1.

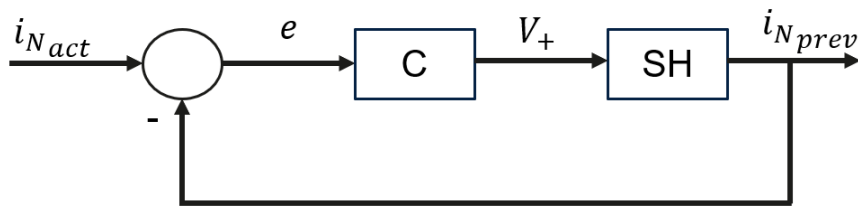


Figure 20. Block diagram of control loop designed.

In Figure 20, the input of the system is the mean value of $i_{N_{act}}$, the actual value i_N currently in the system, sampled at $f_s = 5 \text{ kHz}$ over a time window $T_S = 0.5 \text{ s}$. The input $i_{N_{act}}$ is subtracted from the previous value of $i_{N_{prev}}$, producing the error signal e . The error in the input to the controller block C , which receives the error as input and outputs a control voltage V_+ that the power supply must apply to restore i_N to the setpoint. This voltage is applied to the sprayhead - block SH - , producing a

new mean value of $i_{N_{act}}$ which is provided again as input to the system, repeating the process.

How fast the controller behaves depends greatly of value chosen for its gains: the proportional gain k_p , the derivative gain k_d and the integral gain k_i . For initial tests, we'll attempt to find the best value for these parameters via simple trial and error, in order to get a general idea if this controller would work for this application.

The setup used in this test is shown on Figure 21. We read the current from the power supplies connected to the computer running the algorithm, and therefore no oscilloscopes are necessary. We use the HS camera with microscopic lens to verify visually the EHDA spraying mode of the nozzles.

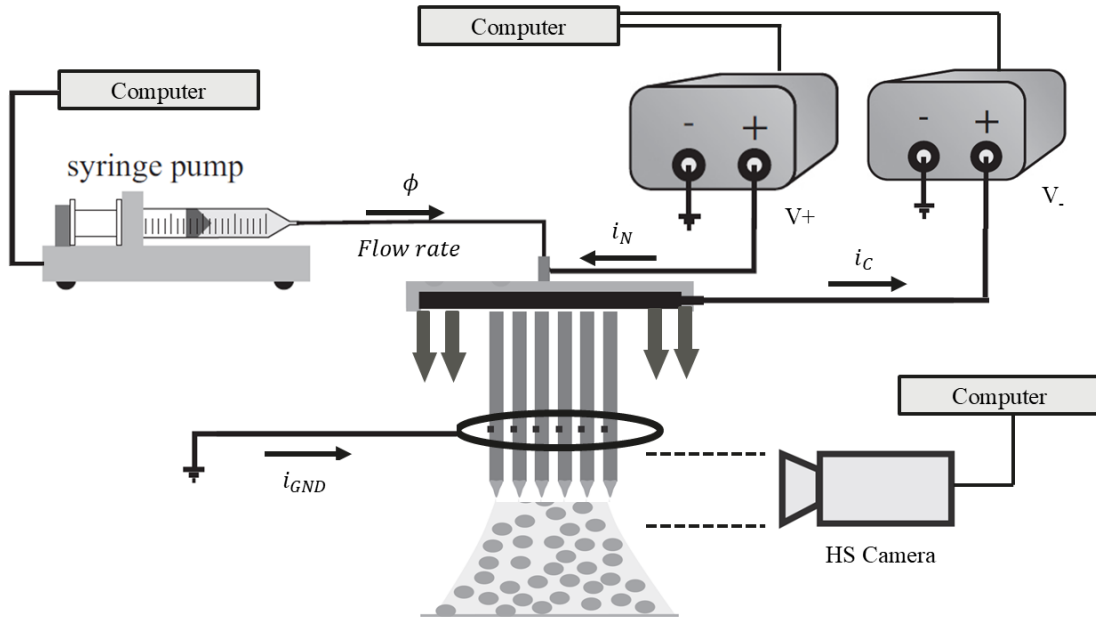


Figure 21. Setup used for PID controller tests.

The result obtained is shown on Figure 22.

As we can see on Figure 22, this initial version of the PID controller is able to autonomously adjust V_+ in order for i_N to reach the setpoint, which in this case was the center of stable region. However, we can see it took about 8 seconds for the current and voltage levels to stabilize. The response time can be improved - i.e. make the controller faster - by changing the gains of the controller, but doing this by trial and error is not feasible. The correct method is to experimentally model the transfer function of the sprayhead in terms of its inputs and outputs, and use this function to obtain the ideal gains based on the time-response requirements.

This method is very time-consuming and complex, and largely falls outside our area of expertise. Therefore, we focused more on the current-based classification and control method discussed on Section 2. Nevertheless, given more time to properly model the transfer function of the sprayhead, the PID controller could be a good candidate for ensuring i_N is always at the stable region.

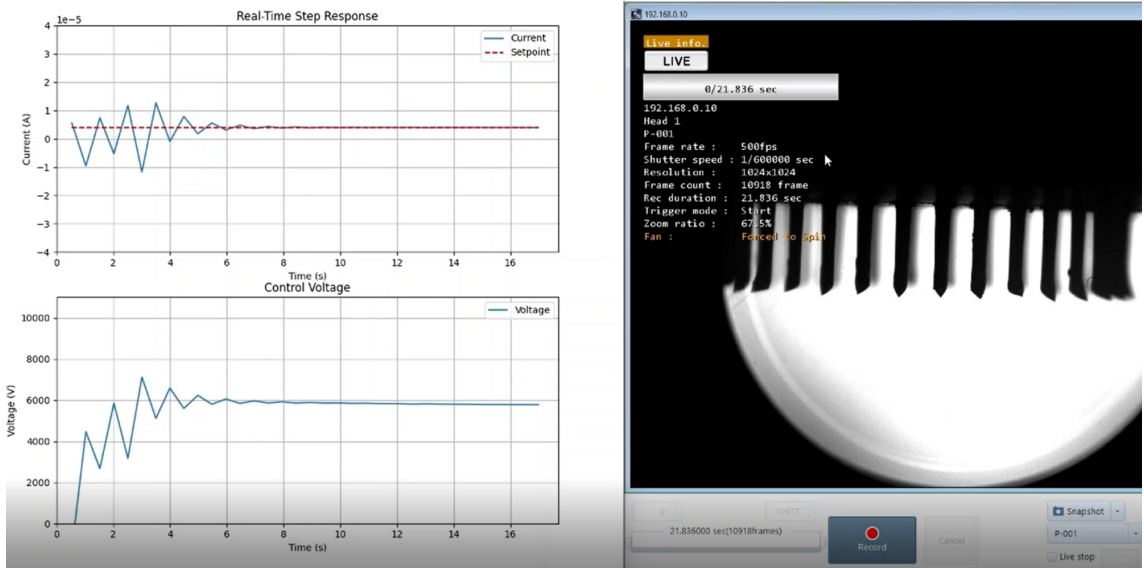


Figure 22. Results of PID controller tests.

4 Other Results

4.1 Flow Rate disturbances

During the PID Controller investigations, we had to analyse possible disturbances that the controller would have to reject. One possible disturbance would be disturbances in ϕ , which Gilbert told us could be in the range of $\pm 10\%$ in the final device. Therefore, using the same setup of Figure 21, we would begin with $\phi = 20 \text{ mL/h}$, and then change the flow rate of the syringe pump mid-operation in two cases:

1. $+100\% \phi$: this is an extreme case to verify the general behaviour of the nozzles with a large change in ϕ
2. $\pm 10\% \phi$: the case given by Gilbert

We used the HS Camera to record and visualize the spraying mode of the nozzles before and after the introduction of the disturbance. The results obtained are shown on Figures 23 and 24.

On Figure 23 (a), the flow rate is $\phi = 30 \text{ mL/h}$ and $i_N = 2 \mu\text{A}$. On $t = 5 \text{ s}$, we change the flow rate to $\phi = 60 \text{ mL/h}$, corresponding to an $+100\%$ change in ϕ . As we can see on Figure 23 (b), the current increases to $i_N = 3 \mu\text{A}$, the cone-jets become visibly more elongated but they are still stable, as well as the mist. The current remains stable in this new value until we return ϕ back to its original value on $t = 20 \text{ s}$, as shown on Figure 24 (a).

On Figure 24 (b), both the cone-jets and i_N return to as they were on Figure 23 (a).

These results show that the sprayhead is very robust when it comes to flow rate disturbances. We repeated the tests for $\pm 10\%$ changes in ϕ and both i_N and the cone-jets barely change at all.



Figure 23. Behaviour of i_N and cone-jets during introduction of ϕ disturbance.



Figure 24. Behaviour of i_N and cone-jets during removal of ϕ disturbance.

4.2 Relations between i_N , i_{GND} and i_C

During the experiments of Figure 4, where the three currents of the system were measured, we found a relation between the values of i_N , i_{GND} and i_C . It appeared that i_C was the sum of i_{GND} and i_N , in the direction defined at Figure 2. In this case, we'd find that

$$i_c = i_N + i_{GND} \quad (3)$$

In order to experimentally verify Equation 3, we defined two parameters:

$$DIFF = i_- - (i_{GND} + i_N) \quad (4)$$

$$DIFF = \frac{i_- - (i_{GND} + i_N)}{i_-} \cdot 100\% \quad (5)$$

Both parameters on Equations 4 and 5 measure how close the difference of both sides of Equation 3 is to zero, which should be case if Equation 3 is true. Calculating the value of these parameters on the data of Figure 4 results in Table 2.

Table 2. Calculated $DIFF$ parameters for the collected data of three currents

Condition	DIFF (nA)	DIFF (%)
Intermittent 20 mL / h	127,43	2,58
Intermittent 30 mL / h	107,66	1,74
Intermittent 50 mL / h	236,09	5,36
Cone-jet 20 mL / h	109,46	1,65
Cone-jet 30 mL / h	34,11	0,80
Cone-jet 50 mL / h	206,49	2,94
Multi-jet 20 mL / h	231,22	3,21
Multi-jet 30 mL / h	38,83	0,41
Multi-jet 50 mL / h	121,08	1,09

As we can see on Table 2, $i_N + i_{GND}$ is always within 5% of the absolute value of i_C , regardless of potential, flow rate or EHDA spray mode. We had discussions of whether or not this could be a useful metric for the control or the charge neutralization measurements, but we did not explore it further. We leave it here if it is something that Gilbert wishes to explore in the future.

4.3 Inrush Current on i_N Measurements

During the work, Gilbert requested us to verify the spike of current on i_N when switching on V_+ . To do this, we used the same setup of Figure 3, only measuring the current i_N with the oscilloscope. V_- was fixed on $V_- = -4.5$ kV, with $\phi = 30$ mL/h. The oscilloscope was configured for $f_s = 50$ kHz to capture the fast response of the inrush current. V_+ was switched on from $V_+ = 0$ to $V_+ = 5$ kV, while V_- was already switched on. Figure 25 shows the result obtained in this test.

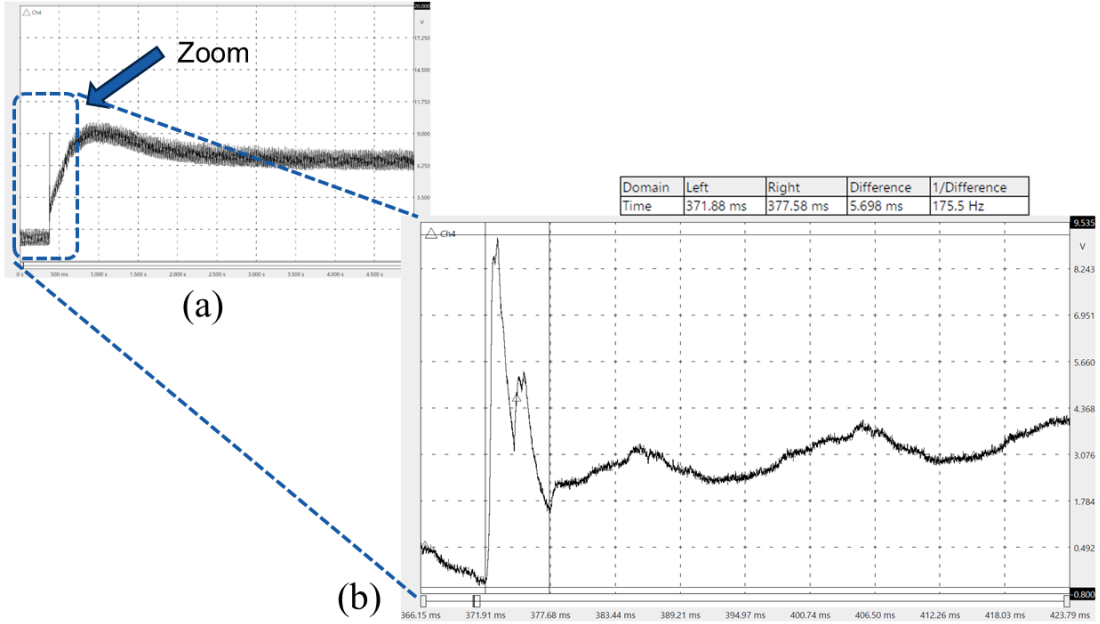


Figure 25. Inrush current measured on i_N (a) over a 5 second time window and (b) with a zoom on the initial spike.

Figure 25 (a) shows that we have a short spike in the current, better viewed on Figure 25 (b). The initial spike lasts for about 6 ms and has a peak value of $i_N = 4 \mu\text{A}$. About 1 second after switching V_+ on, the current achieves its peak overshoot value of $i_N = 4.5 \mu\text{A}$. 2.5 seconds after switching V_+ on the current stabilizes on its final value of $i_N = 3 \mu\text{A}$.

Both peaks of current Figure 25 (a) are about 50% higher than the final value of i_N , and well below the safety threshold of $10 \mu\text{A}$ given by Gilbert. We did not see a large difference on i_N when switching both V_+ and V_- on at the same time.

Notice that the FUG HV power supply accused a very large inrush current on its display, as shown on Figure 26. However, this value contradicts the value given by the oscilloscope, which is a better measurement instrument. In addition, if indeed we had $i_N = 59 \mu\text{A}$ as the FUG displays, it would have resulted in a voltage drop of $\Delta V = 118 \text{ V}$ across the oscilloscope in series with V_+ , which would have fried the channel according to instrument's datasheet. This was not the case, and therefore the physical evidence suggests that the inrush current is indeed as low as the oscilloscope suggests.

4.4 Switching i_N ON and OFF in a 2-second interval

Gilbert also requested us to verify the behaviour of i_N over several switches on V_+ in an interval of 2 seconds. We used the same setup described for Figure 25, obtaining the result shown on Figure 27.

As seen on Figure 27, the inrush current peak is higher for the first time i_N is switched on. After the first time, it is about 50% smaller. The overshoot peak,



Figure 26. Inrush current displayed by the FUG HV power supply.

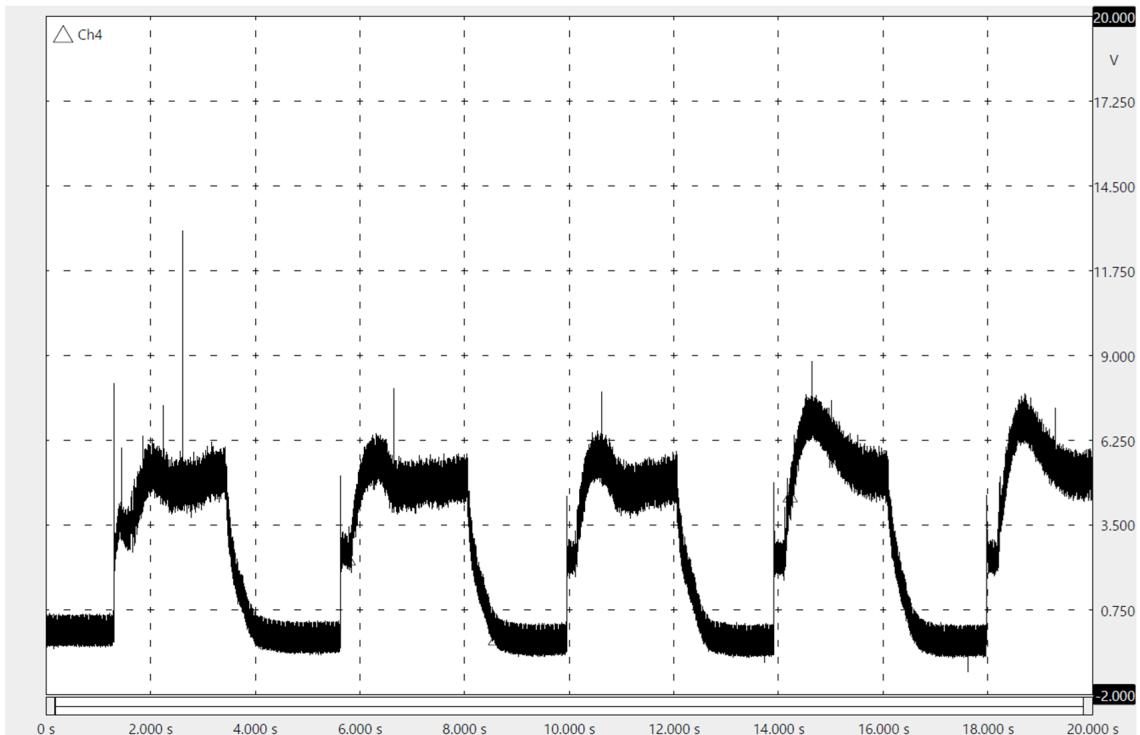


Figure 27. Behaviour of i_N when switching V_+ on and off in a 2-second interval.

however, increases as the system is switched on and off several times. We believe this is caused by the wetness that builds up on the nozzles.

References

- Verdoold, S., Agostinho, L., Yutteri, C., and Marijnissen, J. (2013). A generic electrospray classification. *Journal of Aerosol Science*, 67:87–103.